JACS
JOURNAL OF THE AMERICAN CHEMICAL SOCIETY
Article
Cite This: J. Am. Chem. Soc. 2018, 140, 15290−15299
pubs.acs.org/JACS

Point of Anchor: Impacts on Interfacial Charge Transfer of Metal Oxide Nanoparticles

Yi Peng,[†,§] Bingzhang Lu,[†,§] Feng Wu,[†] Fengqi Zhang,[‡] Jia En Lu,[†] Xiongwu Kang,[‡] Yuan Ping,*[,†] and Shaowei Chen*[,†,‡]

[†]Department of Chemistry and Biochemistry, University of California, 1156 High Street, Santa Cruz, California 95060, United States
[‡]New Energy Research Institute, School of Environment and Energy, South China University of Technology, Guangzhou Higher Education Mega Center, Guangzhou, Guangdong 510006, China

Supporting Information

ABSTRACT: Photoinduced charge transfer across the metal oxide−organic ligand interface plays a key role in the diverse applications of metal oxide nanomaterials/nanostructures, such as photovoltaics, photocatalysis, and optoelectronics. Thus far, most studies are focused on molecular engineering of the organic chromophores, where the charge-transfer properties have been found to dictate the photo absorption efficiency and eventual device performance. Yet, as the chromophores are mostly bound onto the metal oxide surfaces by hydroxyl or carboxyl anchors, the impacts of the bonding interactions at the metal oxide−ligand interface on interfacial charge transfer have remained largely unexplored. Herein, acetylene derivatives are demonstrated as effective surface capping ligands for metal oxide nanoparticles, as exemplified with TiO_2, RuO_2, and ZnO. Experimental studies and first-principles calculations suggest the formation of M−O−C≡C− core−ligand linkages that lead to effective interfacial charge delocalization, in contrast to hopping/tunneling by the conventional M−O−CO− interfacial bonds in the carboxyl-capped counterparts. This leads to the generation of an interfacial state within the oxide bandgap and much enhanced sensitization of the nanoparticle photoluminescence emissions as well as photocatalytic activity, as manifested in the comparative studies with TiO_2 nanoparticles functionalized with ethynylpyrene and pyrenecarboxylic acid. These results highlight the significance of the unique interfacial bonding chemistry by acetylene anchoring group in facilitating efficient charge transfer through the oxide−ligand interfacial linkage and hence the fundamental implication in their practical applications.

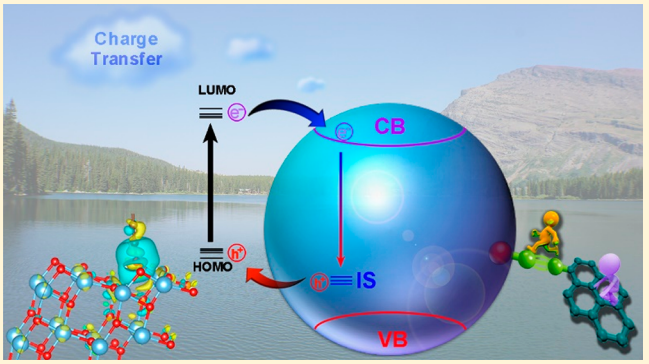

INTRODUCTION

In recent decades, metal oxide nanoparticles have been used extensively in diverse areas, such as catalysis, optoelectronics, bioimaging, and biodiagnosis, owing to their unique optical/electronic properties.[1−5] These properties can be readily regulated by deliberate functionalization with select molecules/ions involving a variety of oxide−ligand interfacial linkages.[6−12] Notably, in these studies, the metal oxide nanoparticle−anchor interactions entail mostly nonconjugated linkages, which limit the coupling between electrons of the nanoparticle core and functional moieties of the capping ligands, resulting in inefficient interfacial charge transfer by hopping/tunneling.[13] For instance, carboxylic acid derivatives represent the most widely used surface capping ligands for metal oxide nanoparticles,[14−21] and several structural models have been proposed to account for the interfacial bonding interactions between COOH and metal oxide surface; yet the exact structural configuration remains under active debates.[22] Phenolic hydroxyl derivatives have also been used for metal oxide surface functionalization through ether-like M−O−R interfacial bonds.[23−30] However, because of the nonconjugated nature of the chemical bonds, interfacial charge transfer is limited. More recently, pyridine and tetrazole moieties have been used as anchors onto metal oxide nanoparticle surfaces by strong coordination between the nitrogen lone pair electrons and Lewis acid sites of the metal oxides; yet the electrons are found to be mostly localized on the heterocycle anchor, rather than delocalized to the metal oxides, leading to inefficient interfacial charge transfer.[31,32]

An immediate question arises. Can the interfacial electron transfer be enhanced by the formation of conjugated covalent linkages? Note that for metal nanoparticles, extensive research has indeed demonstrated that efficient intraparticle charge transfer occurs between the functional moieties adsorbed onto the particle surface via conjugated metal−ligand interfacial bonds.[33−37] For instance, acetylene derivatives can self-assemble onto transition-metal nanoparticle surfaces, forming metal-vinylidene (M═C═CH−) π bonds,[38] where the electronic coupling (H_{ab}) between the electron-donating and

Received: August 2, 2018
Published: October 22, 2018

DOI: 10.1021/jacs.8b08035
J. Am. Chem. Soc. 2018, 140, 15290−15299

-accepting states has been found to significantly increase, as compared to that with saturated interfacial linkages.[39] More recently, photogated intraparticle charge delocalization has also been seen with acetylene-functionalized TiO_2 nanoparticles, suggesting that the oxide-acetylene interfacial bonds behaved analogously to metal-vinylidene conjugated linkages.[40] Yet, thus far, the exact chemical nature of the metal oxide-acetylene bonds has remained largely elusive; and more significantly, it remains unclear whether this is a generic phenomenon among a wide range of transition-metal oxides. The issues are further compounded by two possible anchoring sites of the metal oxides (i.e., the metal and oxygen sites). Resolving the nature of these bonds and their effect on interfacial charge transfer are the primary motivation of the present work.

In this study, stable TiO_2 nanoparticles were synthesized by the functionalization of acetylene derivatives and used as the initial illustrating example to unravel the chemical structure of the interfacial bonding interactions and the impacts on the nanoparticle optical and electronic properties. Results from FTIR and ^{1}H NMR measurements, in combination with density functional theory (DFT) studies, suggested the formation of Ti−O−C≡C− interfacial bonds. Steady-state photoluminescence (SSPL) measurements exhibited an additional emission band beyond the band edge emission, suggesting the formation of an interfacial state (IS) between the TiO_2 valence band (VB) and conduction band (CB). This was confirmed in DFT calculations where the formation of IS was due to charge transfer from the acetylene group (C≡C) of the alkyne ligands to TiO_2 based on Bader charge analysis and charge density redistribution. By contrast, no such IS was formed with the conventional anchors of carboxylic ligands where interfacial charge transfer was essentially blocked. To further illustrate the efficient charge transfer via the Ti−O−C≡C− interfacial bonds, ethynylpyrene was employed to functionalize TiO_2 nanoparticles (TiO_2-EPy). Results showed that the IS emission was readily sensitized by the pyrene groups, as manifested in both SSPL and time-resolved photoluminescence (TRPL) measurements, in sharp contrast with the pyrenecarboxylic acid-functionalized (TiO_2-PyCA) counterpart, leading to much better photocatalytic performance toward methylene blue degradation with TiO_2-EPy than with TiO_2-PyCA. Similar conjugated interfacial bonding interactions, and hence interfacial charge transfer, were observed with other transition-metal oxides, for example, RuO_2 and ZnO. Collectively, these results show that the unique oxide−acetylene interfacial bonding interaction can be exploited as a powerful parameter in the regulation of the optical and electronic properties of metal oxide nanoparticles, a critical step toward their diverse practical applications.

EXPERIMENTAL SECTION

Chemicals. *n*-Octyne (HC8, 98%, Alfa Aesar), ethynylpyrene (EPy, 96%, Alfa Aesar), oleic acid (OA, Spectrum), pyrenecarboxylic acid (PyCA, 97%, TCI America), quinine sulfate (Sigma-Aldrich), *tert*-butylamine (99%, ACROS), titanium(IV) *n*-propoxide (99%, ACROS), and methylene blue (MB, 95%, Acros) were used as received. Solvents were obtained from leading commercial sources at the highest purity available and also used without further treatment. Water was deionized with a Barnstead Nanopure Water System (18.3 MΩ·cm).

Alkyne-Functionalized TiO_2 Nanoparticles. Alkyne-functionalized TiO_2 nanoparticles were synthesized in a biphasic hydrothermal procedure.[40] Briefly, a solution of *tert*-butylamine (50 μL in 5 mL of water) was prepared in a 20 mL Teflon-lined stainless-steel autoclave, into which was then slowly added a mixture of octyne (0.5 mL), titanium(IV) *n*-propoxide (75 mg) and toluene (5.0 mL), forming a two-phase system. The autoclave was sealed and heated at 180 °C for 12 h. After being cooled down to ambient temperature, the toluene phase was separated, and solvents were removed by rotatory evaporation. The obtained solids were washed with methanol for 6 times, affording a final product that was referred to as TiO_2-HC8, which was readily soluble in nonpolar media, for example, CH_2Cl_2, $CHCl_3$, THF, and toluene.

Pyrene-functionalized TiO_2 nanoparticles were synthesized in the same fashion, except that 12 mg of EPy was added into toluene layer along with octyne, such that the resulting TiO_2 nanoparticles were capped by a mixed monolayer of octyne and EPy (and identified as TiO_2-EPy).

The same procedure was also used to prepare two control samples. In the first one, OA (0.5 mL) was used in place of octyne to synthesize OA-protected TiO_2 (TiO_2-OA) nanoparticles. The other entailed the addition of HC8 (0.5 mL) and PyCA (12 mg) to synthesize PyCA and HC8 coprotected TiO_2 (TiO_2-PyCA) nanoparticles.

Characterizations. TEM images were acquired with a Philips CM300 electron microscope operated at 300 kV. FTIR measurements were conducted with a PerkinElmer FTIR spectrometer (in a spectral resolution of 4 cm^{-1}), with the nanoparticle samples deposited onto a ZnSe disk. ^{1}H NMR spectra were collected with a Varian Unity 500 MHz spectrometer using concentrated solutions of the nanoparticles in CD_2Cl_2. UV−vis and SSPL spectra were acquired with a PerkinElmer Lambda 35 UV−vis absorption spectrometer and PTI fluorospectrometer, respectively. TRPL decay spectra were collected on a Horiba QM-3304 instrument at the pulsed laser excitation of 337 nm in the time-correlated single-photon counting (TCSPC) mode.

Photocatalysis. In the photocatalytic degradation of MB by TiO_2-EPy and TiO_2-PyCA, the catalysts (20 mg) prepared above were added into a MB solution in water (50 mL, 10 mg/mL). That is, the loading of catalysts was the same at 0.4 mg/mL. The solution was under magnetic stirring in the dark for 30 min so that adsorption could reach an equilibrium, prior to photoirradiation with a UV lamp (365 nm, 16 W/cm^2). An aliquot of the solution was then removed in the time interval of 2.5 min, and a UV−vis spectrum was recorded until there was no change of the UV profile.

Computational Methods. The open source planewave code, Quantum ESPRESSO, was used in DFT calculations.[41] 1 × 3 supercells were built for TiO_2 (101) of five layers in thickness. To prevent interactions between periodic images, the vacuum thickness was fixed at 12 Å, and to eliminate net dipoles in the cell, the slab models included ligands with inversion symmetry. The ultrasoft pseudopotential[42] was adopted with a 40 Ry cutoff of the kinetic energy and a 240 Ry cutoff of the charge density for the Perdew−Burke−Eernzerhof (PBE) calculations. The optimized norm-conserving Vanderbilt (ONCV) pseudopotential[43] was adopted with a 90 Ry cutoff of the kinetic energy and a 360 Ry cutoff of the charge density for the Heyd−Scuseria−Ernzerhof (HSE06) hybrid functional calculations.[44] The proportion of Hartree−Fock (HF) exchange is set at 22%. The Monkhorst−Pack *K*-points of 4 × 2 × 1 and 2 × 2 × 1 are used for PBE and hybrid functional calculations, respectively. The Marzari−Vanderbilt smearing[45] was used at the smearing of 0.001 Ry for all calculations except for pristine TiO_2. The electronic energy was converged to 10^{-8} Ry and the force to 10^{-4} au. Energy-resolved charge density distribution was analyzed by open source code JDFTx.[46]

RESULTS AND DISCUSSION

TiO_2 nanoparticles were used as the initial illustrating examples. Four samples were prepared by a biphasic hydrothermal method with titanium(IV) *n*-propoxide as the starting precursor along with select organic capping ligands:[40] two functionalized with acetylene derivatives such as *n*-octyne (TiO_2-HC8) and ethynylpyrene (TiO_2-EPy), and the other two capped with carboxylic derivatives such as OA (TiO_2-OA)

DOI: 10.1021/jacs.8b08035
J. Am. Chem. Soc. 2018, 140, 15290−15299

and pyrenecarboxylic acid (TiO_2-PyCA), as schematically illustrated in Figure 1A. The structure of the TiO_2 nanoparticles was first examined by TEM measurements. From the TEM image in Figure 1B, individual TiO_2-HC8 nanoparticles can be readily resolved. In high-resolution TEM measurements (Figure 1C), one can see that the nanoparticles display clearly defined lattice fringes, and the interplanar spacing of 0.35 nm is in good agreement with that of anatase TiO_2 (101) (JCPDS75-1537).[47] Furthermore, the nanoparticle core diameter mostly fell within the narrow range of 3.5−4.5 nm, with 4.0 ± 0.4 nm on average, as manifested in the core size histogram in Figure 1D.

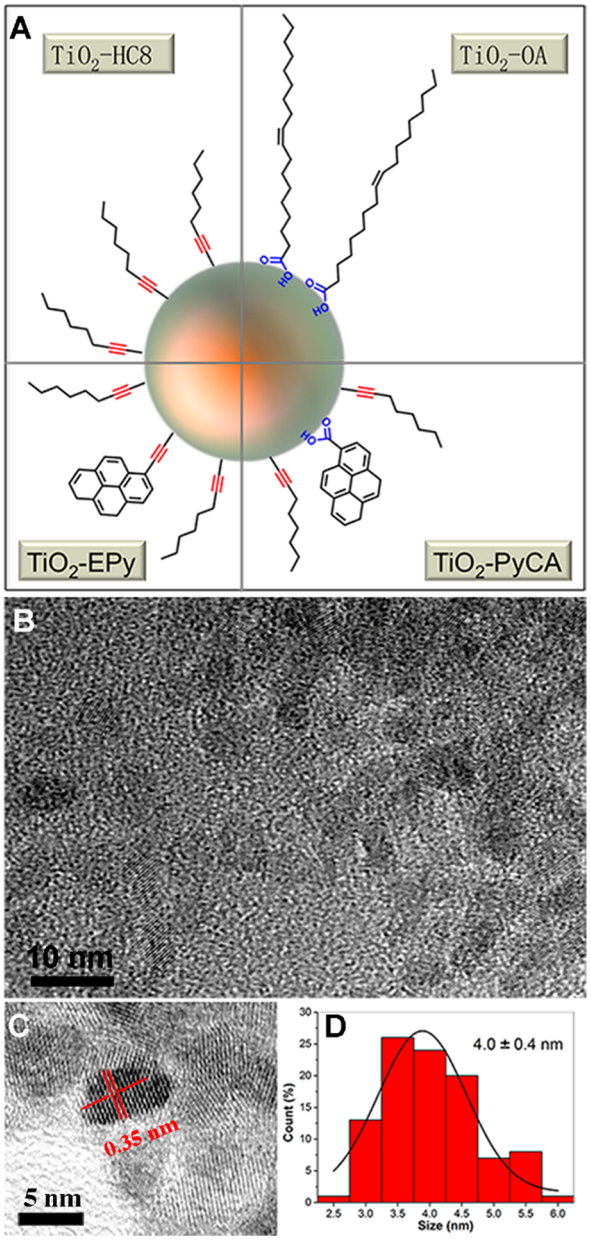

Figure 1. (A) Schematic illustration of four organically functionalized TiO_2 nanoparticles: TiO_2-HC8, TiO_2-OA, TiO_2-EPy, and TiO_2-PyCA. (B−C) Representative TEM images of TiO_2-HC8 nanoparticles and (D) the corresponding core size histogram.

FTIR and ^{1}H NMR measurements were then carried out to characterize the organic capping layers. Figure 2A depicts the FTIR spectra of octyne, EPy, TiO_2-HC8, and TiO_2-EPy. (B) ^{1}H NMR spectra of TiO_2-HC_8 and TiO_2-EPy nanoparticles in CD_2Cl_2. (C) Configuration of the TiO_2-alkyne interface, with the atoms in blue for Ti, red for O, brown for C, and white for H. Inset is the overall configuration of a five-layer TiO_2 model with symmetric ligands on the surface.

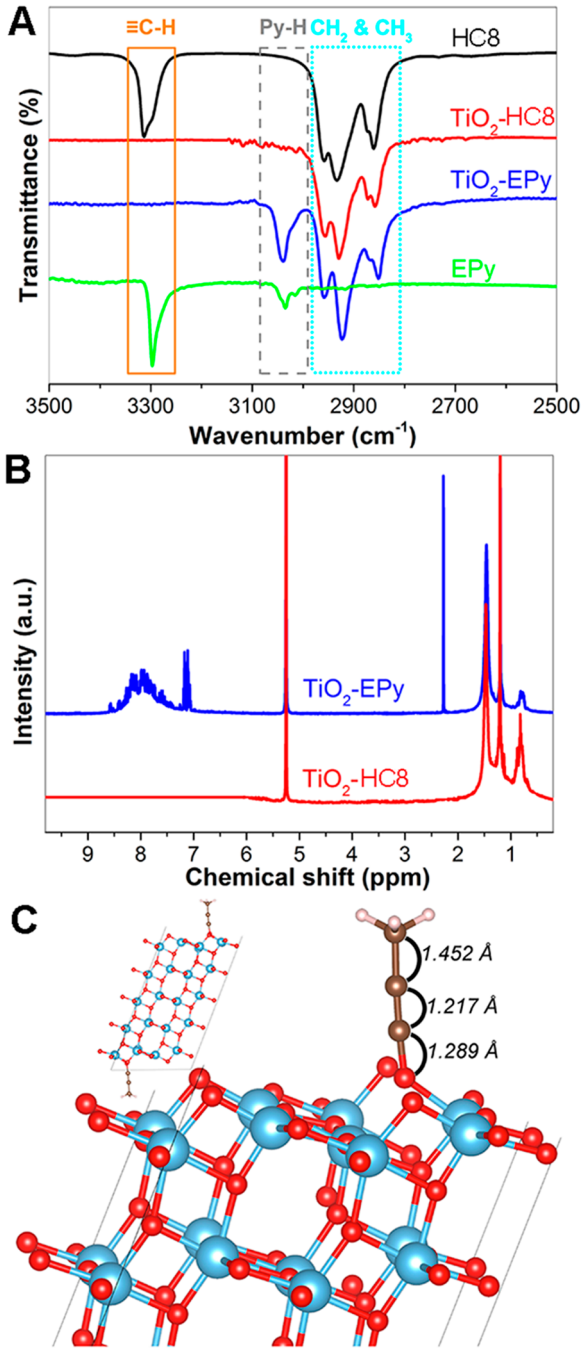

FTIR spectra of TiO_2-HC8 and TiO_2-EPy nanoparticles, along with those of octyne and EPy free monomers. Both nanoparticle samples can be seen to exhibit well-defined vibrational bands at 2958, 2924, 2872, and 2850 cm^{-1}, due to the C−H stretches of CH_2 and CH_3 and consistent with those of monomeric octyne, suggesting that the TiO_2 nanoparticles were indeed successfully capped with the octyne ligands. The TiO_2-EPy sample also exhibited a band at 3040 cm^{-1}, due to the pyrene ring H−C═ vibrational stretch,[48] confirming the incorporation of EPy ligands on the TiO_2 nanoparticle surface.

DOI: 10.1021/jacs.8b08035
J. Am. Chem. Soc. 2018, 140, 15290−15299

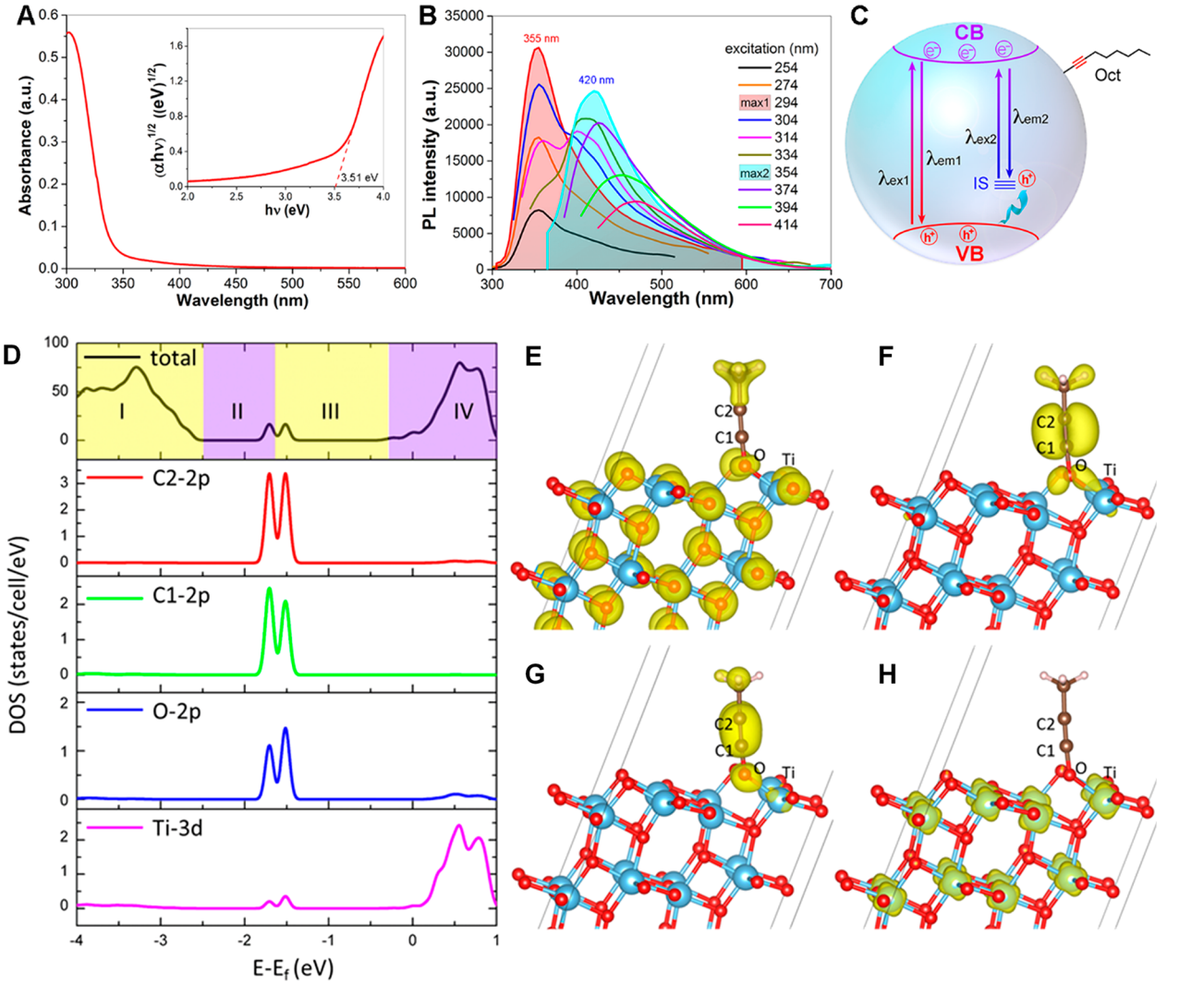

Figure 3. (A) UV−vis spectra of TiO_2-HC8. Inset is the corresponding Tauc plot, with $h\nu$ being the photon energy and α the absorbance. (B) SSPL spectra of TiO_2-HC8 at various excitation wavelengths. The shadowed ones represent maximal emissions at select excitation wavelengths. (C) Schematic illustration of the TiO_2-HC8 band structure based on the SSPL results. (D) TDOS (total density of states) plot of TiO_2−C≡C−CH_3 (black curve) and PDOS plots of the 2p orbitals of C2 (red), C1 (green), and O (blue) atom, and the 3d orbital of the Ti (pink) atom. The corresponding energy-resolved charge density distributions are included in panel (E) for zone I, panel (F) for zone II, panel (G) for zone III, and panel (H) for zone IV. The isovalue is 0.1 e/au^3 for panels (E) and (H) and 0.005 e/au^3 for panels (F) and (G).

Additionally, one can see that octyne and EPy monomers exhibited a prominent vibrational band at 3313 and 3297 cm^{-1}, respectively, arising from the terminal ≡C−H stretch.[49,50] This vibration vanished altogether for TiO_2-HC8 and TiO_2-EPy, due to breaking of the ≡C−H bond when the acetylene derivatives were adsorbed onto the TiO_2 surface. This also indicates that the nanoparticle samples were pure, and excess ligands were removed. Consistent results were obtained in ^{1}H NMR studies. Figure 2B depicts the ^{1}H NMR spectra of the TiO_2-HC8 and TiO_2-EPy nanoparticles in CD_2Cl_2, where the broad peak at 0.89 ppm is due to terminal CH_3 protons of the octyne ligands, whereas the peaks at 1.28 and 1.54 ppm are due to the CH_2 protons. For the TiO_2-EPy sample, an additional broad peak can be identified at 7.35−8.65 ppm for the pyrene ring protons.[48] Furthermore, the mole ratio between the octyne and EPy ligands on the TiO_2 surface was evaluated to be 1:0.66, on the basis of the integrated peak areas. Also, the fact that only broad peaks were observed and the terminal ≡C−H protons cannot be seen in the nanoparticle samples (3.43 ppm for EPy and 2.87 ppm for octyne)[48,51] further confirms the absence of free ligands in the nanoparticle samples, consistent with results from FTIR measurements in Figure 2A (the sharp features at 2.34, 7.15, and 7.24 ppm are due to the methyl and phenyl protons of residual toluene).[52]

To understand the interfacial structure of acetylene-capped TiO_2, we carried out DFT calculations with a fully relaxed five-layer symmetric TiO_2 slab model. The TiO_2 slab is in anatase phase with the (101) lattice surface exposed, according to the experimental results in Figure 1C. To simplify the calculation, the simplest ligand −C≡C−CH_3 was used, and the optimized structure of the supercell and slab surface is shown in Figure 2C and its inset. In the stable configuration, the acetylene carbon atom was found to bind to the oxygen atom, instead of the titanium atom, on the TiO_2 surface, forming a Ti−O−C≡C− interfacial linkage. Note that when we placed the ligand onto the titanium site as the initial configuration, it eventually migrated to the oxygen site after geometric relaxation (Figure S1), suggesting that a Ti−C≡C− interfacial bond is

DOI: 10.1021/jacs.8b08035
J. Am. Chem. Soc. 2018, 140, 15290−15299

energetically unfavorable. Moreover, one can see that in Ti−O−C≡C−, the C−O bond length is 1.289 Å, which is shorter than a carbon−oxygen single bond (1.43 Å) but longer than a double bond (1.23 Å); concurrently, the C≡C bond length became somewhat elongated to 1.217 Å, as compared to that of a free monomer (1.20 Å), whereas the C−C bond shrank slightly to 1.452 Å from 1.47 Å for a Csp^3−Csp single bond.[53] Collectively, these results show that the formation of Ti−O−C≡C− interfacial linkage was likely facilitated by partial charge transfer of the π-electrons in C≡C to TiO_2, leading to shortened and strengthened C−O and C−C bonds at the core−ligand interface.

The apparent coupling between the electrons of the acetylene moiety and TiO_2 nanoparticles leads to new optical properties of the nanoparticle, as manifested in UV−vis and photoluminescence measurements. Figure 3A depicts the UV−vis absorption spectrum of the TiO_2-HC8 nanoparticles, and the bandgap was quantitatively evaluated to be about 3.51 eV from the Tauc plot (Figure 3A inset),[54] Note that this was somewhat larger than that (3.2 eV) of bulk (anatase) TiO_2, likely due to quantum confinement effect, as the average size of the TiO_2 nanoparticles was below the Bohr exciton radius (2.35 nm).[55] Figure 3B shows the corresponding SSPL profiles. One can see that at the excitation (λ_{ex}) of 254 nm, the emission (λ_{em}) peaked at 355 nm (red-shaded). At increasing λ_{ex} (e.g., 304 and 314 nm), an additional emission peak emerged at around 420 nm (2.95 eV, aqua-shaded), and the intensities of these two emission peaks reached the maxima at λ_{ex1} = 294 nm and λ_{ex2} = 354 nm, respectively. Interestingly, despite a very similar band gap energy (ca. 3.2 eV, Figure S2A), TiO_2-OA nanoparticles exhibited only a single emission peak at λ_{em} = 375 nm within a similar range of λ_{ex} (Figure S2B). Therefore, for the TiO_2-HC8 nanoparticles, the emission at λ_{em1} = 355 nm was likely due to TiO_2 band-edge emission, where the energy (3.49 eV) is almost identical to the band gap derived from UV−vis measurements (3.51 eV), while the second emission at λ_{em2} = 420 nm suggests the formation of an IS, due to electronic interactions between the acetylene moiety and TiO_2, as schematically illustrated in Figure 3C.

This is, in fact, confirmed by results from DFT calculations. Figure 3D depicts the plot of density of states (DOS) for a TiO_2 slab. One can see that the band gap (2.2 eV) was somewhat underestimated, as compared to that determined experimentally from Figure 3A (due to the well-known self-interaction errors at the standard PBE level; consistent results were obtained by employing a higher level of theory such as DFT with hybrid functionals HSE06, as shown in Figure S3).[56−58] Yet, upon the adsorption of acetylene derivatives onto the TiO_2 surface, new states are generated within the band gap (zones II and III), consistent with the experimental SSPL results, where a new emission band emerged at 420 nm (Figure 3B) (from Figure S3 one can see that the experimental band gap of bulk TiO_2 was well-reproduced by using more accurate HSE06 hybrid functional to quantify the electronic structure of functionalized TiO_2 slabs). Furthermore, from Figure 3D which depicts the projected density of states (PDOS) plots of the 2p orbitals of C2 (red), C1 (green), and O (blue) atoms and the 3d orbitals of Ti (pink) atom, one can see that the IS is dominated by the 2p orbitals of sp-hybridized carbon (C≡C) and O atoms, with minor contributions from the 3d orbitals of the adjacent Ti atom. Consistent results can be obtained from the plots of charge density distribution within different energy windows, zone I (Figure 3E), zone II (Figure 3F), zone III (Figure 3G), and zone IV (Figure 3H). From Figure 3E and 3H, one can clearly see that the major contributor to the valence band (zone I) is the O atom, whereas contributions to the conduction band (zone IV) are primarily from the Ti atom, which is also manifested by the pink curve (Ti-3d) in Figure 3D. Consistent with PDOS plots in Figure 3D, the IS can be seen from Figure 3F−G to be mainly due to the sp-hybridized carbon, with additional contributions from adjacent oxygen and titanium atoms.

The emergence of IS arising from the formation of Ti−O−C≡C− interfacial linkage was further evidenced by comparing the DOS profiles of pristine and organically modified TiO_2 slabs. From Figure 4, one can see that (i) the bandgap of the

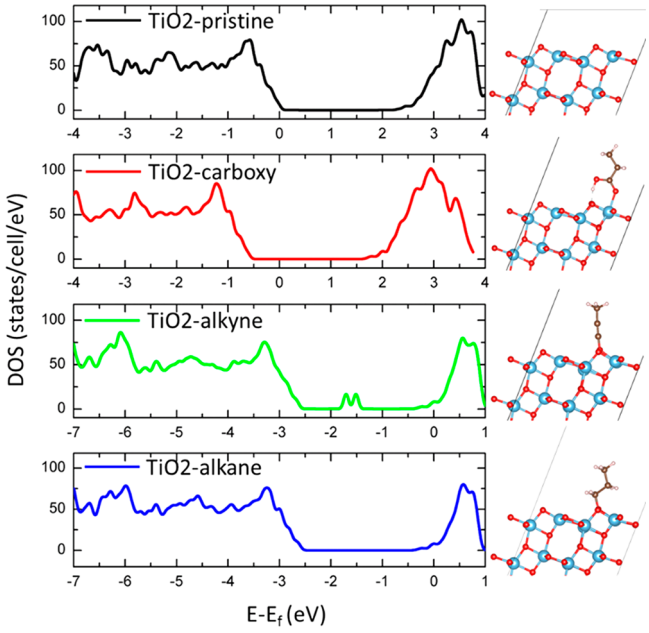

Figure 4. TDOS and interfacial configurations of a pristine TiO_2 slab and a slab functionalized with carboxy (−COOH), alkyne (−C≡C−), and alkane (−CH_2−CH_2−) ligands.

TiO_2 slab remained almost unchanged regardless of surface modification and (ii) the alkyne-functionalized TiO_2 slab exhibited apparent states within the bandgap (green curve), a behavior unseen in pristine TiO_2 (black curve) or TiO_2 slabs modified with carboxyl (red curve) or alkane (blue curve). Note that the results for carboxy-modified TiO_2 are consistent with those of TiO_2-OA (Figure S2), suggesting the formation of Ti−O−C(OH)− linkage in TiO_2-OA,[59] a leading structural model postulated in the literature,[60−62] while alkane-functionalized TiO_2 cannot be verified by experiments due to the lack of effective synthesis methods. Nevertheless, these results clearly indicate that IS formation within the TiO_2 bandgap is due to the unique Ti−O−C≡C− interfacial bonding interactions.

Further insights into the interfacial bonding chemistry can be obtained from analysis of charge distributions within the nanoparticles. From Figure 5A, one can see that there is a large cyan area around the C≡C carbon atoms and adjacent oxygen atom, indicating a significant electron loss from this region, whereas several yellow areas can be identified all over the TiO_2 slab, suggesting electron gain of the Ti and O atoms (of TiO_2). This signifies strong spontaneous charge delocalization from the acetylene moiety to TiO_2. By contrast, no obvious charge

DOI: 10.1021/jacs.8b08035
J. Am. Chem. Soc. 2018, 140, 15290−15299

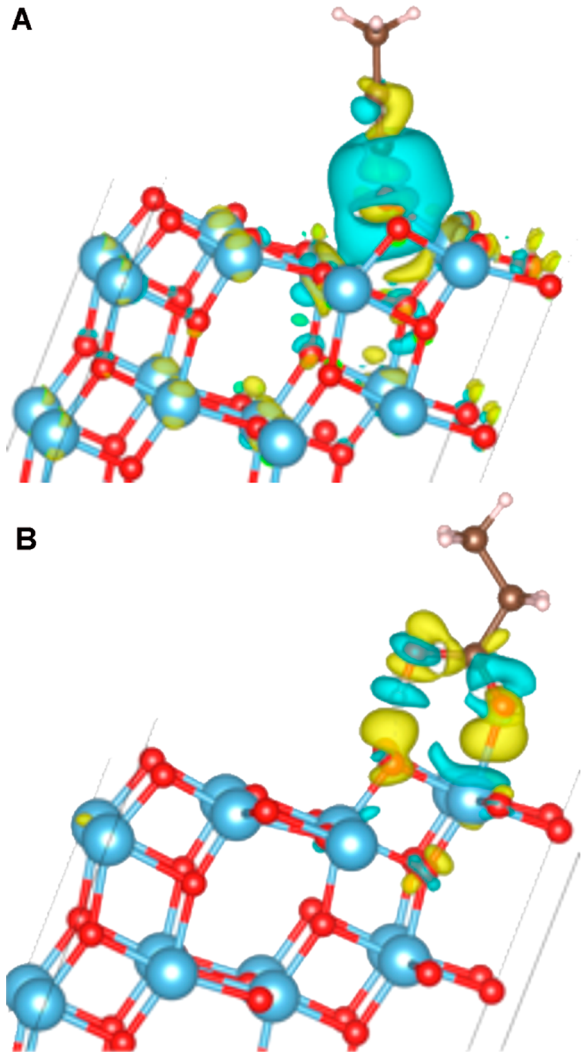

Figure 5. Charge transfer between ligand and TiO_2 slab: (A) TiO_2-alkyne and (B) TiO_2-carboxy. The cyan area indicates electron loss, and yellow area indicates electron gain. The isosurface value is 0.003 e/au^3.

delocalization was observed with carboxy-functionalized TiO_2. From Figure 5B, one can see that almost all the yellow and blue areas are confined to the ligand, indicating that charge delocalization from the ligand to TiO_2 was impeded. This result is in coincidence with the Bader charge analysis (Table S1), where the Bader charge of TiO_2-alkyne is ca. 1.2 electron per ligand from alkyne to TiO_2, while charge transfer is negligible with only ca. 0.01 electron per ligand from TiO_2 to carboxy for the TiO_2-carboxy counterpart. This reflects virtually barrierless charge transfer across the TiO_2-alkyne interface, whereas with the TiO_2-carboxy interfacial linkage, an appreciable driving force is needed to facilitate interfacial charge transfer that is mostly hopping/tunneling in nature. Note that the level of theory and the slab models used in the above calculations were validated by comparing results using slab models of various layers of TiO_2 with HSE06 exchange–correlation functional (Figures S4–S5 and Table S1), which showed very good agreement with the band gap of TiO_2 estimated experimentally. In addition, constrained DFT calculations[63] of TiO_2-alkyne and TiO_2-carboxy clusters (Figure S6) show that the electronic coupling (H_{ab}) between TiO_2 and the end ligand of the former is ca. 5 times that of the latter. As it is likely that the shape and relative position of the potential energy surfaces of TiO_2 and the end ligand (such as EPy) are not changed by the relatively small bridging anchor group (i.e., the reorganization energy and driving force in the Marcus' theory remain unchanged by the bridging anchor group), the increased H_{ab} indicates a lower charge-transfer barrier and a higher transfer rate (detailed discussion can be found in the SI below Figure S6). Note that we added an excess electron to the system for the calculation of H_{ab} between TiO_2 and the end ligand, which is related to excited electron transfer between them. Collectively, these results show that the formation of Ti–O–C≡C– bonding linkage significantly facilitated interfacial charge transfer.

This is actually a general phenomenon for a wide range of transition-metal oxides, as manifested in further studies with RuO_2 and ZnO. These two oxides were chosen because of the unique electronic structures of the metal centers, zinc(II) with a full d-electron subshell and ruthenium(IV) with a half-full d-electron subshell, in comparison with Ti(IV) in TiO_2 that has an empty d-electron subshell. From DFT calculations, it can be seen that (i) both oxide nanoparticles also showed a stable structure with the alkyne ligands bonded to the oxygen atoms, instead of the metal atoms (ZnO-alkyne in Figure S7A, and RuO_2-alkyne in Figure S7B), consistent with results for TiO_2-alkyne (Figure 5A) and (ii) there is an apparent charge transfer of 1.10 and 1.43 electrons from the alkyne ligand to ZnO and RuO_2 (cyan area), respectively, also comparable to that (1.2 electrons) for TiO_2-alkyne. By contrast, charge transfer from carboxylic ligands to ZnO and RuO_2 was negligible at only 0.06, and 0.64 electron (Figure S7C–D), respectively, very similar to that (0.01 electron) for TiO_2-carboxy (Figure 5B). Collectively, these results show that (i) acetylene derivatives can indeed serve as effective capping ligands for the surface functionalization of a wide range of metal oxide nanoparticles and (ii) the formation of conjugated M–O–C≡C– interfacial linkages facilitates apparent charge transfer between the acetylene moiety and metal oxide, in contrast to conventional capping ligands (e.g., carboxylic derivatives) where charge transfer across the core–ligand interface is negligible. This may have significant implication in practical applications of these oxide nanomaterials, as demonstrated below.

One can envisage that if a suitable electron donor is bound onto a metal oxide nanoparticle via the M–O–C≡C– linkage, effective charge transfer occurs from the electron-donating moiety to the metal oxide, which leads to the emergence of new optical and electronic properties. By contrast, such interfacial charge transfer will be impeded with a carboxy anchor. Herein, pyrene is exploited as a molecular probe to highlight the significance of such interfacial bonding linkages in the control of nanoparticle interfacial charge transfer and optical and electronic properties. Two samples, TiO_2-EPy and TiO_2-PyCA were prepared and compared (Figure 1A). Figure 6A depicts the UV–vis absorption spectra of EPy and TiO_2-EPy. The EPy monomers can be seen to exhibit four prominent peaks at 314, 328, 343, and 360 nm, due to the $S_0 \rightarrow S_n$ transitions of the pyrene π electrons;[64] consistent absorption features can also be observed with TiO_2-EPy, though with a slight red-shift of 4 to 7 nm, likely due to enhanced interactions between the pyrene moieties, as they were in close proximity on the nanoparticle surface, akin to the situation of pyrene-containing polymers.[65] Furthermore, in comparison to TiO_2-HC8, one can see that TiO_2-EPy showed a diminishment of the effective bandgap to 2.94 eV (Figure 6A

DOI: 10.1021/jacs.8b08035
J. Am. Chem. Soc. 2018, 140, 15290–15299

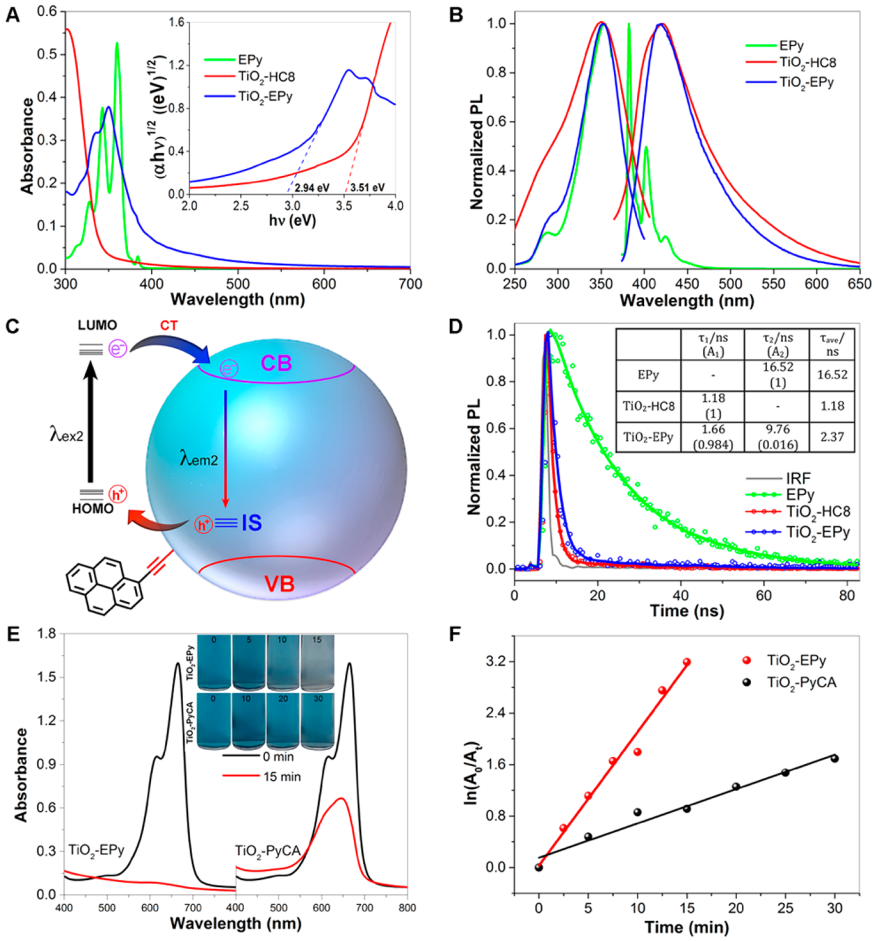

Figure 6. (A) UV−vis spectra of monomeric EPy, TiO_2-HC8, and TiO_2-EPy. Inset shows the corresponding Tauc plots. (B) Normalized steady-state excitation and emission spectra of monomeric EPy, TiO_2-HC8, and TiO_2-EPy. (C) Schematic of charge transfer at the Ti−O−C≡C-Py interface. (D) TRPL decay profiles of monomeric EPy, TiO_2-HC8, and TiO_2-EPy. The gray curve is the background of the instrument response function (IRF). The experimental data (symbols) are fitted with either a monoexponential or biexponential function (solid curves). Results of the fitting are summarized in the inset table. (E) UV−vis spectra of a MB solution before and after UV photoirradiation for 15 min using TiO_2-EPy or TiO_2-PyCA as catalysts. The inset shows the photographs of the solution at different times (in min). (F) Variation of MB peak absorbance with photoirradiation time. The experimental results (symbols) are fitted by linear regressions.

inset), suggesting enhancement of visible absorption, in comparison to pristine TiO_2. This is likely because electronic transition involving the IS became dominant thanks to the formation of Ti−O−C≡C− interfacial bonds.

This distinction is also manifested in SSPL measurements. Form Figure 6B, it can be seen that monomeric EPy exhibited three characteristic emissions at 382, 402, and 425 nm[64] and rapidly decayed in intensity with an increase of the excitation wavelength (Figure S8A). By contrast, TiO_2-EPy displayed only a single, broad emission centered at λ_{em} = 420 nm, independent of the excitation wavelength (Figure S8B). Note that this emission peak position is the same as λ_{em2} of TiO_2-HC8 (Figure 3B), suggesting that it arose from the radiative recombination of CB electrons and IS holes of TiO_2 (Figure 3C). In addition, the photoluminescence quantum yield (ϕ) of TiO_2-EPy was estimated to be 36.6%, using quinine sulfate (in 0.1 M H_2SO_4) as the standard (ϕ = 54%),[66] which is markedly higher than that of TiO_2-HC8 (6.9%). This can be ascribed to charge donation from the pyrene group to TiO_2 CB and the subsequent radiative decay to the IS holes, leading to marked sensitization of the TiO_2 IS emission, consistent with results from UV−vis (Figure 6A) and DFT calculations (Figure 3D). Based on the above data, the electronic structure of TiO_2-EPy is schematically illustrated in Figure 6C. For comparison, TiO_2-PyCA nanoparticles, with the pyrene moiety anchored onto the TiO_2 surface through the COOH moiety (Figure 1A), no apparent variation was observed in the SSPL profile, as compared with that of monomeric PyCA (Figure S9A−D), because of the lack of electronic coupling between the ligand and the oxide core. In a further control experiment with a physical mixture of TiO_2-HC8 nanoparticles and monomeric EPy, we observed that the corresponding SSPL profile was identical to that of EPy monomers (Figure S9E), negating the possibility of Förster resonance energy transfer in the TiO_2-EPy system.

The electron-transfer dynamics from pyrene to the TiO_2−alkyne interface (Ti−O−C≡C−) were also investigated by TRPL measurements. Figure 6D shows the normalized decay profiles after pulsed laser excitation at 337 nm for the series of samples (the gray curve is the background of the instrument response function, IRF). Note that at this excitation, the emission of TiO_2-HC8 and TiO_2-EPy is dominated by λ_{em2} (Figure 3B). The data may be fitted by either single- or double-exponential decay kinetics,[67] $I(t) = A_1e^{-t/\tau_1} + A_2e^{-t/\tau_2}$, where $A_1 + A_2 = 1$, and the fitting

DOI: 10.1021/jacs.8b08035
J. Am. Chem. Soc. 2018, 140, 15290−15299

parameters are listed in the inset of Figure 6D. For monomeric EPy, the data were fitted by a monoexponential function, and the decay time constant (τ) was estimated to be ca. 16.52 ns, consistent with results observed earlier with pyrene derivatives,[64] due to the recombination of S_n excited electrons to S_0 holes of pyrene. TiO_2-HC8 nanoparticles also showed a single decay lifetime, which was markedly shorter at 1.18 ns for the recombination of excited electrons at CB to IS holes. The fact that both EPy and TiO_2-HC8 showed only a single photoluminescence pathway is in good agreement with results from the SSPL measurements (Figure 6B). For TiO_2-EPy nanoparticles where the TiO_2 cores were cofunctionalized with octyne and EPy ligands, the data were fitted by a double-exponential equation, and two lifetimes were identified at τ_1 = 1.66 ns and τ_2 = 9.76 ns. The long component is consistent with the slow decay of pyrene, while the short lifetime was close to that of TiO_2-HC8 and might be attributed to the fast decay of IS. Moreover, the contributions of the fast and slow decay components were estimated to be 98.4% and 1.6%, respectively, suggesting that the dominant pathway for electron transfer entailed excited electrons on TiO_2 CB to IS. Again, this is in agreement with the SSPL results, where the quenching of pyrene emission and the enhancement of IS emission were attributed to the efficient electron transfer from pyrene to TiO_2 CB. Additionally, the average lifetime $\langle\tau\rangle$ can be calculated by $\langle\tau\rangle = \frac{A_1\tau_1^2 + A_2\tau_2^2}{A_1\tau_1 + A_2\tau_2}$ and was found to be 2.37 ns for TiO_2-EPy, which is somewhat higher than that of TiO_2-HC8. Furthermore, the electron-transfer rate constant (k_{et}), which can be estimated by $k_{et} = \frac{1}{\langle\tau\rangle_{TiO_2\text{-EPy}}} - \frac{1}{\langle\tau\rangle_{EPy}}$, was 3.61×10^8 s^{-1}, indicating fast charge-transfer kinetics from pyrene to TiO_2 CB. For comparison, TiO_2-PyCA, where the pyrene moiety was anchored onto the TiO_2 surface by a carboxyl linker instead (Figure 1A), the lifetime remained almost invariant, as compared to that of monomeric PyCA (τ = 6.13 ns) (Figure S9F), because of impeded charge transfer at the core−ligand interface.

In theoretical simulation, we applied phenylacetylene as a simplified representation of EPy in TiO_2-EPy to bind onto the surface of a TiO_2 slab (Figure S10A). The DOS plot (Figure S10B) suggests that IS remained visible, and an additional gap state emerged due to the conjugation between the phenyl ring (representing EPy) and the C≡C moiety. By contrast, no obvious IS was formed with aromatic derivatives that featured a COOH anchor.[59] These results are consistent with the experimental data described above.

Such unique interfacial bonding interactions markedly impact the nanoparticle photocatalytic activity, as manifested in the photocatalytic degradation of MB by TiO_2-EPy and TiO_2-PyCA. Figure 6E shows the UV−vis absorption spectra of a MB solution (10 mg/L) containing the same amount of catalysts (0.4 mg/L) before and after 15 min of UV photoirradiation (365 nm, 16 W/cm^2). It can be seen that MB was almost completely degraded in 15 min by TiO_2-EPy, while only 55% by TiO_2-PyCA (Figure 6E inset), although the absorbance at 365 nm was slightly higher with TiO_2-PyCA than with TiO_2-EPy (Figure S11A). In fact, from Figure 6F and Figure S11B, one can see that the degradation rate constant for TiO_2-EPy (0.208 min^{-1}) is ∼4 times that for TiO_2-PyCA (0.054 min^{-1}) and ∼15 times that for TiO_2-HC8 (0.014 min^{-1}). This indicates that the enhanced photocatalytic performance of TiO_2-EPy is due to sensitization by the pyrene groups through the acetylene linkage.

CONCLUSION

Results presented herein clearly demonstrate that acetylene derivatives can serve as effective capping ligands for metal oxide nanoparticles, and the resultant M−O-C≡C- interfacial linkages lead to markedly enhanced electronic coupling between the ligand π electrons and metal-oxide cores, whereas interfacial charge transfer is significantly impeded with conventional anchor groups such as the carboxy moiety. This suggests that with a deliberate manipulation of the nanoparticle interfacial point of anchor, the optical and electronic properties of the metal-oxide nanoparticles can be regulated at an unprecedented level of sophistication, a variable that has remained largely unexplored thus far. This will have significant implication in their diverse practical applications, such as photovoltaics, photocatalysis, and photodynamic therapeutics.

ASSOCIATED CONTENT

Supporting Information

The Supporting Information is available free of charge on the ACS Publications website at DOI: 10.1021/jacs.8b08035.

Additional computational and spectroscopic data (PDF)

AUTHOR INFORMATION

Corresponding Authors

*shaowei@ucsc.edu

*yuanping@ucsc.edu

ORCID

Yi Peng: 0000-0002-5319-1336

Xiongwu Kang: 0000-0003-2587-4962

Yuan Ping: 0000-0002-0123-3389

Shaowei Chen: 0000-0002-3668-8551

Author Contributions

§These authors contributed equally.

Notes

The authors declare no competing financial interest.

ACKNOWLEDGMENTS

This work was supported, in part, by the National Science Foundation (CHE-1710408, S.W.C.; DMR-1760260, Y. Ping). Y. Ping also acknowledges support of a Hellman Fellowship. The authors thank the National Center for Electron Microscopy at the Lawrence Berkeley National Laboratory, which is supported by the US Department of Energy, for access to the TEM facilities. Part of the calculations were carried out with the Extreme Science and Engineering Discovery Environment (XSEDE) that is supported by the National Science Foundation (ACI-1548562).[68] This research also used resources of the Center for Functional Nanomaterials, which is a U.S. DOE Office of Science Facility, and the Scientific Data and Computing Center, a component of the Computational Science Initiative, at Brookhaven National Laboratory under Contract No. DE-SC0012704, as well as resources of the National Energy Research Scientific Computing Center (NERSC) that is supported by the Office of Science of the US Department of Energy under Contract No. DEAC02-05CH11231. The authors also thank Mr. D. States for the assistance in manuscript preparation.

DOI: 10.1021/jacs.8b08035
J. Am. Chem. Soc. 2018, 140, 15290−15299

REFERENCES

(1) Long, M. C.; Brame, J.; Qin, F.; Bao, J. M.; Li, Q. L.; Alvarez, P. J. J. Phosphate Changes Effect of Humic Acids on TiO2 Photocatalysis: From Inhibition to Mitigation of Electron-Hole Recombination. *Environ. Sci. Technol.* **2017**, *51* (1), 514−521.

(2) Youngblood, W. J.; Lee, S. H. A.; Kobayashi, Y.; Hernandez-Pagan, E. A.; Hoertz, P. G.; Moore, T. A.; Moore, A. L.; Gust, D.; Mallouk, T. E. Photoassisted Overall Water Splitting in a Visible Light-Absorbing Dye-Sensitized Photoelectrochemical Cell. *J. Am. Chem. Soc.* **2009**, *131* (3), 926−927.

(3) Yella, A.; Lee, H. W.; Tsao, H. N.; Yi, C. Y.; Chandiran, A. K.; Nazeeruddin, M. K.; Diau, E. W. G.; Yeh, C. Y.; Zakeeruddin, S. M.; Gratzel, M. Porphyrin-Sensitized Solar Cells with Cobalt (II/III)-Based Redox Electrolyte Exceed 12% Efficiency. *Science* **2011**, *334* (6056), 629−634.

(4) Yang, J. B.; Ganesan, P.; Teuscher, J.; Moehl, T.; Kim, Y. J.; Yi, C. Y.; Comte, P.; Pei, K.; Holcombe, T. W.; Nazeeruddin, M. K.; Hua, J. L.; Zakeeruddin, S. M.; Tian, H.; Gratzel, M. Influence of the Donor Size in D-pi-A Organic Dyes for Dye-Sensitized Solar Cells. *J. Am. Chem. Soc.* **2014**, *136* (15), 5722−5730.

(5) Kairdolf, B. A.; Smith, A. M.; Stokes, T. H.; Wang, M. D.; Young, A. N.; Nie, S. M. Semiconductor Quantum Dots for Bioimaging and Biodiagnostic Applications. *Annu. Rev. Anal. Chem.* **2013**, *6*, 143−162.

(6) Ardo, S.; Meyer, G. J. Photodriven heterogeneous charge transfer with transition-metal compounds anchored to TiO2 semiconductor surfaces. *Chem. Soc. Rev.* **2009**, *38* (1), 115−164.

(7) Silvi, S.; Credi, A. Luminescent sensors based on quantum dot-molecule conjugates. *Chem. Soc. Rev.* **2015**, *44* (13), 4275−4289.

(8) Gao, X. H.; Cui, Y. Y.; Levenson, R. M.; Chung, L. W. K.; Nie, S. M. In vivo cancer targeting and imaging with semiconductor quantum dots. *Nat. Biotechnol.* **2004**, *22* (8), 969−976.

(9) Greenham, N. C.; Peng, X. G.; Alivisatos, A. P. Charge separation and transport in conjugated-polymer/semiconductor-nanocrystal composites studied by photoluminescence quenching and photoconductivity. *Phys. Rev. B: Condens. Matter Mater. Phys.* **1996**, *54* (24), 17628−17637.

(10) Heinz, H.; Pramanik, C.; Heinz, O.; Ding, Y. F.; Mishra, R. K.; Marchon, D.; Flatt, R. J.; Estrela-Lopis, I.; Llop, J.; Moya, S.; Ziolo, R. F. Nanoparticle decoration with surfactants: Molecular interactions, assmbly, and applications. *Surf. Sci. Rep.* **2017**, *72* (1), 1−58.

(11) Duncan, W. R.; Prezhdo, O. V. Theoretical studies of photoinduced electron transfer in dye-sensitized TiO(2). *Annu. Rev. Phys. Chem.* **2007**, *58*, 143−184.

(12) Mathew, S.; Yella, A.; Gao, P.; Humphry-Baker, R.; Curchod, B. F. E.; Ashari-Astani, N.; Tavernelli, I.; Rothlisberger, U.; Nazeeruddin, M. K.; Gratzel, M. Dye-sensitized solar cells with 13% efficiency achieved through the molecular engineering of porphyrin sensitizers. *Nat. Chem.* **2014**, *6* (3), 242−247.

(13) Vura-Weis, J.; Abdelwahed, S. H.; Shukla, R.; Rathore, R.; Ratner, M. A.; Wasielewski, M. R. Crossover from Single-Step Tunneling to Multistep Hopping for Molecular Triplet Energy Transfer. *Science* **2010**, *328*, 1547−1500.

(14) Asghar, M. I.; Miettunen, K.; Halme, J.; Vahermaa, P.; Toivola, M.; Aitola, K.; Lund, P. Review of stability for advanced dye solar cells. *Energy Environ. Sci.* **2010**, *3* (4), 418−426.

(15) Hagfeldt, A.; Boschloo, G.; Sun, L. C.; Kloo, L.; Pettersson, H. Dye-Sensitized Solar Cells. *Chem. Rev.* **2010**, *110* (11), 6595−6663.

(16) Sodeyama, K.; Sumita, M.; O'Rourke, C.; Terranova, U.; Islam, A.; Han, L.; Bowler, D. R.; Tateyama, Y. Protonated Carboxyl Anchor for Stable Adsorption of Ru N749 Dye (Black Dye) on a TiO2 Anatase (101) Surface. *J. Phys. Chem. Lett.* **2012**, *3* (4), 472−7.

(17) Ashford, D. L.; Song, W.; Concepcion, J. J.; Glasson, C. R.; Brennaman, M. K.; Norris, M. R.; Fang, Z.; Templeton, J. L.; Meyer, T. J. Photoinduced electron transfer in a chromophore-catalyst assembly anchored to TiO2. *J. Am. Chem. Soc.* **2012**, *134* (46), 19189−98.

(18) Hu, K.; Robson, K. C. D.; Johansson, P. G.; Berlinguette, C. P.; Meyer, G. J. Intramolecular Hole Transfer at Sensitized TiO2 Interfaces. *J. Am. Chem. Soc.* **2012**, *134* (20), 8352−8355.

(19) Chen, H. Y.; Ardo, S. Direct observation of sequential oxidations of a titania-bound molecular proxy catalyst generated through illumination of molecular sensitizers. *Nat. Chem.* **2018**, *10* (1), 17−23.

(20) Ye, S.; Kathiravan, A.; Hayashi, H.; Tong, Y. J.; Infahsaeng, Y.; Chabera, P.; Pascher, T.; Yartsev, A. P.; Isoda, S.; Imahori, H.; Sundstrom, V. Role of Adsorption Structures of Zn-Porphyrin on TiO2 in Dye-Sensitized Solar Cells Studied by Sum Frequency Generation Vibrational Spectroscopy and Ultrafast Spectroscopy. *J. Phys. Chem. C* **2013**, *117* (12), 6066−6080.

(21) Long, R.; Casanova, D.; Fang, W. H.; Prezhdo, O. V. Donor−Acceptor Interaction Determines the Mechanism of Photoinduced Electron Injection from Graphene Quantum Dots into TiO2: π-Stacking Supersedes Covalent Bonding. *J. Am. Chem. Soc.* **2017**, *139* (7), 2619−2629.

(22) Galoppini, E. Linkers for anchoring sensitizers to semiconductor nanoparticles. *Coord. Chem. Rev.* **2004**, *248* (13−14), 1283−1297.

(23) Kamegawa, T.; Matsuura, S.; Seto, H.; Yamashita, H. A Visible-Light-Harvesting Assembly with a Sulfocalixarene Linker between Dyes and a Pt-TiO2 Photocatalyst. *Angew. Chem., Int. Ed.* **2013**, *52* (3), 916−919.

(24) Amstad, E.; Gillich, T.; Bilecka, I.; Textor, M.; Reimhult, E. Ultrastable Iron Oxide Nanoparticle Colloidal Suspensions Using Dispersants with Catechol-Derived Anchor Groups. *Nano Lett.* **2009**, *9* (12), 4042−4048.

(25) Rajh, T.; Chen, L. X.; Lukas, K.; Liu, T.; Thurnauer, M. C.; Tiede, D. M. Surface restructuring of nanoparticles: An efficient route for ligand-metal oxide crosstalk. *J. Phys. Chem. B* **2002**, *106* (41), 10543−10552.

(26) Lana-Villarreal, T.; Rodes, A.; Perez, J. M.; Gomez, R. A spectroscopic and electrochemical approach to the study of the interactions and photoinduced electron transfer between catechol and anatase nanoparticles in aqueous solution. *J. Am. Chem. Soc.* **2005**, *127* (36), 12601−12611.

(27) Notestein, J. M.; Iglesia, E.; Katz, A. Photoluminescence and charge-transfer complexes of calixarenes grafted on TiO2 nanoparticles. *Chem. Mater.* **2007**, *19* (20), 4998−5005.

(28) Park, Y.; Singh, N. J.; Kim, K. S.; Tachikawa, T.; Majima, T.; Choi, W. Fullerol-Titania Charge-Transfer-Mediated Photocatalysis Working under Visible Light. *Chem. - Eur. J.* **2009**, *15* (41), 10843−10850.

(29) Xu, C. J.; Xu, K. M.; Gu, H. W.; Zheng, R. K.; Liu, H.; Zhang, X. X.; Guo, Z. H.; Xu, B. Dopamine as a robust anchor to immobilize functional molecules on the iron oxide shell of magnetic nanoparticles. *J. Am. Chem. Soc.* **2004**, *126* (32), 9938−9939.

(30) Marczak, R.; Werner, F.; Gnichwitz, J. F.; Hirsch, A.; Guldi, D. M.; Peukert, W. Communication via Electron and Energy Transfer between Zinc Oxide Nanoparticles and Organic Adsorbates. *J. Phys. Chem. C* **2009**, *113* (11), 4669−4678.

(31) Ooyama, Y.; Inoue, S.; Nagano, T.; Kushimoto, K.; Ohshita, J.; Imae, I.; Komaguchi, K.; Harima, Y. Dye-Sensitized Solar Cells Based On Donor-Acceptor pi-Conjugated Fluorescent Dyes with a Pyridine Ring as an Electron-Withdrawing Anchoring Group. *Angew. Chem., Int. Ed.* **2011**, *50* (32), 7429−7433.

(32) Massin, J.; Ducasse, L.; Toupance, T.; Olivier, C. Tetrazole as a New Anchoring Group for the Functionalization of TiO2 Nanoparticles: A Joint Experimental and Theoretical Study. *J. Phys. Chem. C* **2014**, *118* (20), 10677−10685.

(33) Ciampi, S.; Harper, J. B.; Gooding, J. J. Wet chemical routes to the assembly of organic monolayers on silicon surfaces via the formation of Si-C bonds: surface preparation, passivation and functionalization. *Chem. Soc. Rev.* **2010**, *39* (6), 2158−2183.

(34) Hu, P. G.; Chen, L. M.; Kang, X. W.; Chen, S. W. Surface Functionalization of Metal Nanoparticles by Conjugated Metal-Ligand Interfacial Bonds: Impacts on Intraparticle Charge Transfer. *Acc. Chem. Res.* **2016**, *49* (10), 2251−2260.

DOI: 10.1021/jacs.8b08035
J. Am. Chem. Soc. 2018, 140, 15290−15299

(35) Chen, W.; Chen, S. W.; Ding, F. Z.; Wang, H. B.; Brown, L. E.; Konopelski, J. P. Nanoparticle-mediated intervalence transfer. *J. Am. Chem. Soc.* **2008**, *130* (36), 12156−12162.
(36) Hu, P. G.; Chen, L. M.; Deming, C. P.; Kang, X. W.; Chen, S. W. Nanoparticle-Mediated Intervalence Charge Transfer: Core-Size Effects. *Angew. Chem., Int. Ed.* **2016**, *55* (4), 1455−1459.
(37) Zhou, T. L.; Anderson, R. T.; Li, H. S.; Bell, J.; Yang, Y. A.; Gorman, B. P.; Pylypenko, S.; Lusk, M. T.; Sellinger, A. Bandgap Tuning of Silicon Quantum Dots by Surface Functionalization with Conjugated Organic Groups. *Nano Lett.* **2015**, *15* (6), 3657−3663.
(38) Kang, X. W.; Zuckerman, N. B.; Konopelski, J. P.; Chen, S. W. Alkyne-Functionalized Ruthenium Nanoparticles: Ruthenium-Vinylidene Bonds at the Metal-Ligand Interface. *J. Am. Chem. Soc.* **2012**, *134* (3), 1412−1415.
(39) Ding, F. Z.; Wang, H. B.; Wu, Q.; Van Voorhis, T.; Chen, S. W.; Konopelski, J. P. Computational Study of Bridge-Assisted Intervalence Electron Transfer. *J. Phys. Chem. A* **2010**, *114* (19), 6039−6046.
(40) Peng, Y.; Lu, J. E.; Deming, C. P.; Chen, L. M.; Wang, N.; Hirata, E. Y.; Chen, S. W. Photo-Gated Intervalence Charge Transfer of Ethynylferrocene Functionalized Titanium Dioxide Nanoparticles. *Electrochim. Acta* **2016**, *211*, 704−710.
(41) Giannozzi, P.; Baroni, S.; Bonini, N.; Calandra, M.; Car, R.; Cavazzoni, C.; Ceresoli, D.; Chiarotti, G. L.; Cococcioni, M.; Dabo, I.; et al. QUANTUM ESPRESSO: a modular and open-source software project for quantum simulations of materials. *J. Phys.: Condens. Matter* **2009**, *21* (39), 395502.
(42) Garrity, K. F.; Bennett, J. W.; Rabe, K. M.; Vanderbilt, D. Pseudopotentials for high-throughput DFT calculations. *Comput. Mater. Sci.* **2014**, *81*, 446−452.
(43) Hamann, D. Optimized norm-conserving Vanderbilt pseudopotentials. *Phys. Rev. B: Condens. Matter Mater. Phys.* **2013**, *88* (8), 085117.
(44) Heyd, J.; Scuseria, G. E.; Ernzerhof, M. Hybrid functionals based on a screened Coulomb potential. *J. Chem. Phys.* **2003**, *118* (18), 8207−8215.
(45) Marzari, N.; Vanderbilt, D.; De Vita, A.; Payne, M. Thermal contraction and disordering of the Al (110) surface. *Phys. Rev. Lett.* **1999**, *82* (16), 3296.
(46) Sundararaman, R.; Letchworth-Weaver, K.; Schwarz, K. A.; Gunceler, D.; Ozhabes, Y.; Arias, T. A. JDFTx: Software for joint density-functional theory. *SoftwareX* **2017**, *6*, 278−284.
(47) Liu, K.; Song, Y.; Chen, S. W. Defective TiO2-supported Cu nanoparticles as efficient and stable electrocatalysts for oxygen reduction in alkaline media. *Nanoscale* **2015**, *7* (3), 1224−1232.
(48) Rivera, E.; Belletete, M.; Zhu, X. X.; Durocher, G.; Giasson, R. Novel polyacetylenes containing pendant 1-pyrenyl groups: synthesis, characterization, and thermal and optical properties. *Polymer* **2002**, *43* (19), 5059−5068.
(49) Rivera, E.; Wang, R. P.; Zhu, X. X.; Zargarian, D.; Giasson, R. Preparation of cis-poly(1-ethynylpyrene) using (1-Me-indenyl)-(PPh3)Ni-C C-Ph/methylaluminoxane as catalyst. *J. Mol. Catal. A: Chem.* **2003**, *204*, 325−332.
(50) Hu, P. G.; Song, Y.; Chen, L. M.; Chen, S. W. Electrocatalytic activity of alkyne-functionalized AgAu alloy nanoparticles for oxygen reduction in alkaline media. *Nanoscale* **2015**, *7* (21), 9627−9636.
(51) Terekhov, D. S.; Nolan, K. J. M.; McArthur, C. R.; Leznoff, C. C. Synthesis of 2,3,9,10,16,17,23,24-octaalkynylphthalocyanines and the effects of concentration and temperature on their H-1 NMR spectra. *J. Org. Chem.* **1996**, *61* (9), 3034−3040.
(52) Fulmer, G. R.; Miller, A. J. M.; Sherden, N. H.; Gottlieb, H. E.; Nudelman, A.; Stoltz, B. M.; Bercaw, J. E.; Goldberg, K. I. NMR Chemical Shifts of Trace Impurities: Common Laboratory Solvents, Organics, and Gases in Deuterated Solvents Relevant to the Organometallic Chemist. *Organometallics* **2010**, *29* (9), 2176−2179.
(53) Allen, F. H.; Kennard, O.; Watson, D. G.; Brammer, L.; Orpen, A. G.; Taylor, R. Tables of Bond Lengths Determined by X-Ray and Neutron-Diffraction 0.1. Bond Lengths in Organic-Compounds. *J. Chem. Soc., Perkin Trans. 2* **1987**, No. 12, S1−S19.
(54) Serpone, N.; Lawless, D.; Khairutdinov, R. Size Effects on the Photophysical Properties of Colloidal Anatase Tio2 Particles - Size Quantization or Direct Transitions in This Indirect Semiconductor. *J. Phys. Chem.* **1995**, *99* (45), 16646−16654.
(55) Hormann, U.; Kaiser, U.; Albrecht, M.; Geserick, J.; Husing, N. Structure and luminescence of sol-gel synthesized anatase nanoparticles. *J. Phys: Conf Ser.* **2010**, *209*, 012039.
(56) Thulin, L.; Guerra, J. Calculations of strain-modified anatase TiO 2 band structures. *Phys. Rev. B: Condens. Matter Mater. Phys.* **2008**, *77* (19), 195112.
(57) Patrick, C. E.; Giustino, F. GW quasiparticle bandgaps of anatase TiO2 starting from DFT+ U. *J. Phys.: Condens. Matter* **2012**, *24* (20), 202201.
(58) Wang, Y.; Zhang, H.; Liu, P.; Yao, X.; Zhao, H. Engineering the band gap of bare titanium dioxide materials for visible-light activity: a theoretical prediction. *RSC Adv.* **2013**, *3* (23), 8777−8782.
(59) Martsinovich, N.; Jones, D. R.; Troisi, A. Electronic Structure of TiO2 Surfaces and Effect of Molecular Adsorbates Using Different DFT Implementations. *J. Phys. Chem. C* **2010**, *114* (51), 22659−22670.
(60) Yao, Z.; Zhang, M.; Wu, H.; Yang, L.; Li, R.; Wang, P. Donor/acceptor indenoperylene dye for highly efficient organic dye-sensitized solar cells. *J. Am. Chem. Soc.* **2015**, *137* (11), 3799−3802.
(61) Wei, H.; Luo, J.-W.; Li, S.-S.; Wang, L.-W. Revealing the Origin of Fast Electron Transfer in TiO2-Based Dye-Sensitized Solar Cells. *J. Am. Chem. Soc.* **2016**, *138* (26), 8165−8174.
(62) Long, R.; Casanova, D.; Fang, W.-H.; Prezhdo, O. V. Donor−Acceptor Interaction Determines the Mechanism of Photoinduced Electron Injection from Graphene Quantum Dots into TiO2: π-Stacking Supersedes Covalent Bonding. *J. Am. Chem. Soc.* **2017**, *139* (7), 2619−2629.
(63) Goldey, M. B.; Brawand, N. P.; Voros, M.; Galli, G. Charge Transport in Nanostructured Materials: Implementation and Verification of Constrained Density Functional Theory. *J. Chem. Theory Comput.* **2017**, *13* (6), 2581−2590.
(64) Amelia, M.; Lavie-Cambot, A.; McClenaghan, N. D.; Credi, A. A ratiometric luminescent oxygen sensor based on a chemically functionalized quantum dot. *Chem. Commun.* **2011**, *47* (1), 325−327.
(65) Li, X. G.; Liu, Y. W.; Huang, M. R.; Peng, S.; Gong, L. Z.; Moloney, M. G. Simple Efficient Synthesis of Strongly Luminescent Polypyrene with Intrinsic Conductivity and High Carbon Yield by Chemical Oxidative Polymerization of Pyrene. *Chem. - Eur. J.* **2010**, *16* (16), 4803−4813.
(66) Briscoe, J.; Marinovic, A.; Sevilla, M.; Dunn, S.; Titirici, M. Biomass-derived carbon quantum dot sensitizers for solid-state nanostructured solar cells. *Angew. Chem., Int. Ed.* **2015**, *54* (15), 4463−8.
(67) Yun, H. J.; Paik, T.; Edley, M. E.; Baxter, J. B.; Murray, C. B. Enhanced Charge Transfer Kinetics of CdSe Quantum Dot-Sensitized Solar Cell by Inorganic Ligand Exchange Treatments. *ACS Appl. Mater. Interfaces* **2014**, *6* (5), 3721−3728.
(68) Towns, J.; Cockerill, T.; Dahan, M.; Foster, I.; Gaither, K.; Grimshaw, A.; Hazlewood, V.; Lathrop, S.; Lifka, D.; Peterson, G. D.; et al. XSEDE: accelerating scientific discovery. *Comput. Sci. Eng.* **2014**, *16* (5), 62−74.

DOI: 10.1021/jacs.8b08035
J. Am. Chem. Soc. 2018, 140, 15290−15299